RSC Advances

PAPER

View Article Online
View Journal | View Issue

Cite this: *RSC Adv.*, 2023, **13**, 28564

MoS_2–NiO nanocomposite for H_2S sensing at room temperature†

Shama Sadaf,[a] Hongpeng Zhang*[a] and Ali Akhtar *[b]

The layered 2-D materials, such as molybdenum disulfide (MoS_2), are among the most promising candidates for detecting H_2S gas at very low concentrations. Herein, we have designed a series of novel nanocomposites consisting of MoS_2 and NiO. These materials were synthesized *via* a simple hydrothermal method. The microstructure and morphology of nanocomposites were studied using different characterization techniques, such as X-ray diffraction (XRD), scanning electron microscopy (SEM), transmission electron microscopy (TEM), high-resolution transmission electron microscopy (HRTEM), Brunauer–Emmett–Teller (BET) analysis, and X-ray photoelectron spectroscopy (XPS). These nanocomposites were used as gas sensors, and the highest response (6.3) towards 10 ppm H_2S was detected by the MNO-10 gas sensor among all the tested sensors. The response value (R_g/R_a) was almost three times that of pure NiO ($R_g/R_a = 2$). Besides, the MNO-10 sensor exposed good selectivity, short response/recovery time (50/20 s), long-term stability (28 days), reproducibility (6 cycles), and a low detection limit (2 ppm) towards H_2S gas at RT. The excellent performance of MNO-10 may be attributed to some features of MoS_2, such as a layered structure, higher BET surface area, higher active sites, and a synergistic effect between MoS_2 and NiO. This simple fabrication sensor throws a novel idea for detecting H_2S gas.

Received 2nd August 2023
Accepted 14th September 2023

DOI: 10.1039/d3ra05241a

rsc.li/rsc-advances

1. Introduction

Detecting hazardous and flammable volatile organic compounds (VOCs), such as hydrogen sulfide (H_2S), having rotten eggs smell is important for protecting human health. The excessive inhalation of H_2S, around 250 ppm, may cause the death of human beings.[1] A very low concentration of H_2S can cause various chronic diseases, such as poor memory, throat injury, dizziness, cough, and damage to the human nervous system.[2] In this regard, H_2S gas sensors with high response and low limit of detection (LOD) are highly required.

Semiconductor metal oxides (SMOs) are highly recommended and studied as gas sensors because of their advantages of low cost, simple fabrication, and ability to synthesize various nanocomposites.[3] Up to now, different p-type SMOs, such as nickel oxide (NiO), tin oxide (SnO_2), nickel cobaltite ($NiCo_2O_4$), zinc cobaltite ($ZnCo_2O_4$), and zinc oxide (ZnO), have received wide attention in the field of gas sensors[4–8] and supercapacitors.[9] Among these SMOs, cubic NiO, having a band-gap of 3.5 eV, can be used to design novel nanocomposites with different metal oxides due to its marvelous properties, such as electrical, chemical, and thermal stabilities. NiO was found to be a promising candidate for detecting various gases, such as ozone,[10] acetone,[11] H_2S,[12] NH_3,[13] and formaldehyde.[14] However, the reported NiO gas sensors still need improvement due to some demerits, such as high temperature, low response, and poor selectivity. Designing novel nanocomposites of NiO with layered 2-D materials is crucial to achieving these objectives.

MoS_2, an n-type semiconductor having a band-gap of 1.29 eV, is one of the most well-known 2-D transition material dichalcogenides, and especially the layered structures of 2-D materials have received considerable attention because of their strong adsorption, high reactivity, larger surface area to volume ratio, and good electrical conductivity.[15] Except for the gas sensors, it has been used in many fields, such as photo-catalysis,[16] supercapacitors,[17] and lithium-ion batteries.[18] Other 2-D materials also find novel applications as gas sensors[19–22] and supercapacitors.[23] However, MoS_2 can easily be composited with various SMOs to design novel electronic devices; these features make MoS_2 a very promising candidate for detecting hazardous VOCs at low concentrations. In particular, Bai *et al.* proposed a sensor based on the hetero-structure of MoS_2/SnO_2, which exposed the gas sensing properties towards NO_2 at room temperature. The optimized sensor showed a high response, short response/recovery time, good stability, and selectivity. Besides, many sensors, such as MoS_2/SnO_2 (CO sensor),[24] CuO/MoS_2 (NO_2 sensor),[25] MoS_2/ZnO (NO_2 sensor),[26] Au/MoS_2 (NO_2 sensor),[27] MoS_2/ZnO–Zn_2SnO_4 (H_2S sensor),[28] and PtO_2/MoS_2

[a]*Marine Engineering College, Dalian Maritime University, Dalian, 116026, China. E-mail: zhppeter@dlmu.edu.cn; Tel: +86 411 84729934*

[b]*School of Information Science and Technology, Dalian Maritime University, Dalian 116026, Liaoning, P. R. China*

† Electronic supplementary information (ESI) available. See DOI: https://doi.org/10.1039/d3ra05241a

(NH_3 sensor),[29] have been exploited to investigate sub-ppm level gases.

Herein, a series of novel nanocomposites based on NiO spherical nanoparticles and layered MoS_2 were designed for detecting toxic gases. Numerous characterizations such as XRD, SEM, TEM, HRTEM, BET, and XPS were performed for these nanocomposites. The gas sensing properties of the proposed MNO-10 sensor suggested a high response, good selectivity, short response/recovery time, and reliable long-term stability towards 10 ppm H_2S among all other tested sensors (MNO-0, MNO-5, and MNO-15).

2. Experimental section

2.1 Materials

All the chemicals used in the synthesis method were bought from Sinopharm Chemical Reagent Co., Ltd. (Shanghai, China). The materials such as molybdenum disulfide (MoS_2), nickel chloride hexahydrate ($NiCl_2 \cdot 6H_2O$), and sodium hydroxide (NaOH) were utilized in the synthesis method without further purification.

2.2 Synthesis of NiO spherical nanoparticles and nanocomposites of MoS_2–NiO

NiO spherical nanoparticles and nanocomposites with different contents of MoS_2 were subsequently synthesized *via* a simple hydrothermal method, and the details are expressed in Fig. 1. Initially, $NiCl_2 \cdot 6H_2O$ (1.5 g) was mixed with 50 mL deionized water (DI) in four different beakers; after half an hour of stirring, various contents of MoS_2 such as 0.00 g, 0.0505 g, 0.101 g, and 0.151 g were dispersed in all four suspensions. These samples were named MNO-0, MNO-5, MNO-10, and MNO-15, respectively. After that, 2 M NaOH was added to adjust pH = 12. The samples were stirred for 24 h, then the next day, the mixtures were settled in 50 mL stainless steel autoclaves, and the oven was set for 24 h at the operating temperature of 180 °C. The obtained products were washed with DI and ethanol three times using centrifugation. After drying (12 h, 100 °C), the products were calcined at the operating temperature of 350 °C for 2 h and 2 °C min^{-1}. The dried samples, after calcination, were ground in a mortar for different characterizations such as XRD, SEM, and TEM. All these tests were performed by providing various amounts of samples, such as 20–30 mg, 10 mg, 10 mg, 200 mg, and 5–20 mg powder, for XRD, SEM, TEM, BET, and XPS, respectively.

2.3 Fabrication of a sensor

The gas sensor diagram is shown in Fig. 1. The fabrication of sensors was reported in a previous work.[6] After calcination, the paste to fabricate the sensor was prepared using 0.1 g powder and 2 drops of terpineol (the volume was approximately 0.1–0.2 mL for each drop of terpineol) and ground in a mortar. After that, the paste was coated onto the outer surface of an alumina tube with a small brush and then heated the alumina tube in an oven for 2 h at 80 °C. The purpose of the Ni–Cr heating wire was to control the operating temperature. Pt wires were given to link the alumina tube to the gas sensor device. All the hazardous gases detected in the present work were bought from Dalian Haide Technology Company Limited. NiO is a p-type material, and the response was calculated, such as the ratio of gas sensor resistance in gas (R_g) to that of the resistance in air (R_a) ($S = R_g/R_a$). Other important parameters, such as selectivity, stability, reproducibility, limit of detection (LOD), and response/recovery time, are discussed in this paper.

2.4 Physical characterization of materials

The micro-structural properties and morphologies of the synthesized products were observed by X-ray diffraction (XRD, D/MAX-Ultima, Cu Kα source, 2° min^{-1} scanning rate and the scanning angle from 10° to 80° as well as the power was 40 kV and 40 mA, Rigaku, Tokyo, Japan), scanning electron microscopy (SEM, ZEISS Gemini 500, Carl Zeiss AG, Oberkochen, Germany), transmission electron microscopy (TEM, JEM-3200FS, JEOL, Tokyo, Japan), high-resolution transmission electron microscopy (HRTEM, JEM-2100F, JEOL, Tokyo, Japan). Besides, X-ray photoelectron spectroscopy and Brunauer–

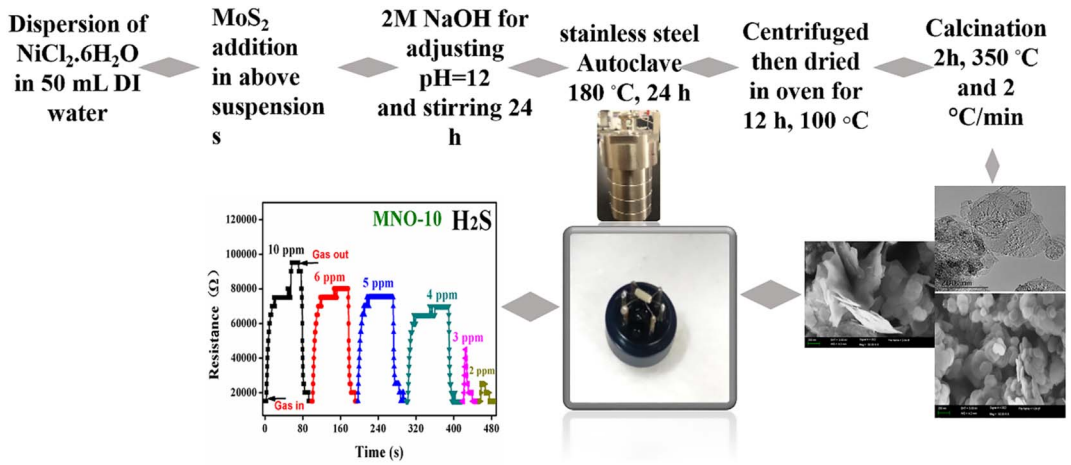

Fig. 1 Synthesis diagram of MoS_2–NiO nanocomposites.

Emmett–Teller analysis were carried out using XPS, ESCALAB 250XI, Thermo Fisher Scientific, Waltham, MA, USA and BET, ASAP2010C instrument, Norcross GA, USA, respectively.

3. Experimental results and discussion

3.1 Morphology and structure

The crystalline nature of the synthesized products was observed using XRD diffraction peaks, as exposed in Fig. 2. The diffraction peaks observed from the patterns corresponded to the crystallographic standard database files of MoS_2 and NiO. The XRD diffraction patterns of all the samples showed the diffraction peaks of NiO at the 2θ values of 37.24°, 43.27°, 62.87°, and 75.41°, corresponding to (111), (200), (220), and (311) planes of NiO (JCPDS no. 47-1049), respectively. Except for the diffraction peaks of MNO-0, one high-intensity MoS_2 peak and two small peaks were observed in all other nanocomposites at 2θ values of 14.37°, 39.53°, and 49.78°, which matched with (002), (103) and (105) planes of MoS_2 (JCPDS no. 37-1492). No extra peaks were found in all patterns, suggesting that the samples were well-ordered and possessed good crystallinity and clarity. Besides, crystallite sizes of NiO spherical nanoparticles in all nanocomposites were calculated using the Debye–Scherrer formula, yielding 15.59, 10.86, 9.36, and 10.07 nm based on the (200) peaks, while 14.02, 10.23, 9.98, and 9.39 nm based on the (111) peak in the nanocomposites of MNO-0, MNO-5, MNO-10, and MNO-15, respectively. It was found that adding MoS_2 in the nanocomposites decreased the crystallite size of NiO.

Fig. 3 reveals the SEM images of all the nanocomposites. The spherical NiO nanoparticles with an average particle size of 150–200 nm are seen from the SEM images of MNO-0 in Fig. 3(a) and (b). The SEM images of the nanocomposite MNO-5 in Fig. 3(c) and (d) and SEM images of the nanocomposite MNO-10 and MNO-15 are displayed in Fig. 3(e)–(h), respectively. Fig. 3(i) shows the SEM image of MoS_2 displaying the layered structure. From SEM images, first of all, the morphology of layered MoS_2 and spherical nanoparticles NiO were observed; secondly, it was noticed that the particle size of NiO was reduced by adding MoS_2 in MNO-5, MNO-10, and MNO-15 nanocomposites. SEM results corresponded to XRD results, which stated that by adding MoS_2 to the samples, the crystallite sizes of NiO were reduced. The uniform scattering of all the elements present in MNO-10 and EDS spectrum is disclosed in Fig. 3(j).

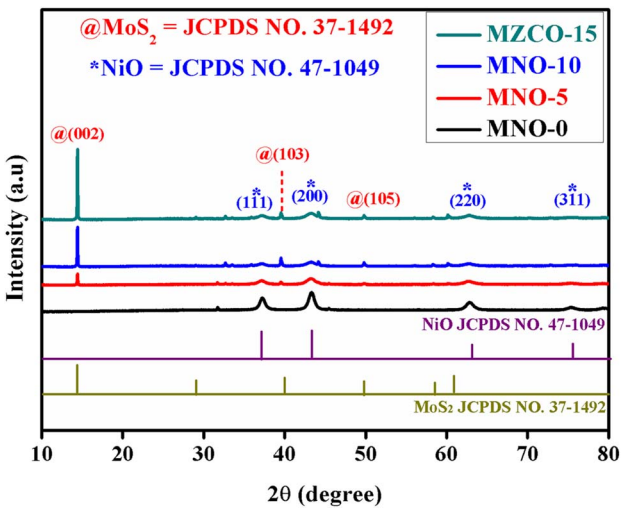

Fig. 2 XRD patterns of MoS_2–NiO nanocomposites.

The decoration of NiO spherical nanoparticles onto the layered structure of MoS_2 was further verified by TEM and HRTEM images. In Fig. 4(a) and (b), TEM images of MNO-0 are disclosed, which showed the average particle size (150–200 nm) of spherical NiO nanoparticles; besides, the clear lattice fringes with a lattice spacing of $d = 0.21$ nm corresponded to the (200) plane of NiO nanoparticles. Also, in Fig. 4(c)–(h), TEM images proved the layered structure of MoS_2 and spherical nanoparticles of NiO, and HRTEM images exposed lattice spacing's of $d = 0.62$ and $d = 0.21$ nm related to the (002) and (311) planes of MoS_2 and NiO nanoparticles. In Fig. 4(i), the layered structure of MoS_2 was verified by TEM analysis. TEM and HRTEM revealed the particle sizes of NiO (150–200 nm). Gradually, their size was reduced by adding MoS_2 contents in the nanocomposite, corresponding to the XRD results.

In Fig. 5, the nitrogen adsorption–desorption isotherms were analyzed for the MNO-0, MNO-5, MNO-10, and MNO-15 nanocomposites to interpret their porosity and distribution. Nitrogen adsorption–desorption isotherms reveal the specific surface area of all the nanocomposites. A higher BET surface area corresponds to a higher gas-sensing response. BET surface areas of nanocomposites of MNO-0, MNO-5, MNO-10, and MNO-15, as shown in Fig. 5(a), were 62.07 $m^2\ g^{-1}$, 70.23 $m^2\ g^{-1}$, 82.44 $m^2\ g^{-1}$ and 89.52 $m^2\ g^{-1}$, respectively. Besides, in the images of Fig. 5(b), the pore size distribution diagrams are seen, suggesting that all the nanocomposites have an obvious H3 hysteresis loop, which verified the presence of many pores as well as the mesoporous nature of samples.[30] It was found that pore volumes and pore sizes of MNO-0, MNO-5, MNO-10, and MNO-15 were 0.2346 $cm^3\ g^{-1}$, 0.2093 $cm^3\ g^{-1}$, 0.3034 $cm^3\ g^{-1}$, 0.2254 $cm^3\ g^{-1}$, and 15.12 nm, 11.92 nm, 14.73 nm, 10.07 nm, respectively. Due to the higher BET surface areas and wide pore size distributions of nanocomposites, these were denoted as high gas sensing responsive, especially the gas sensor of MNO-10, which detected high response towards 10 ppm H_2S.

The surface chemical composition and electronic state of MNO-0 and MNO-10 nanocomposites were measured using X-ray photoelectron spectroscopy. The details are as follows: in Fig. 6(a), the full scan XPS spectrum is given, which specifies the presence of elements such as Ni, O, M, and S in the MNO-10 nanocomposite. Next, the high-resolution spectrum of Ni 2p is displayed in Fig. 6(b). The two peaks in the spectrum of MNO-10 at 854.9 eV and 872.8 eV corresponded to Ni $2p_{3/2}$ and Ni $2p_{1/2}$,[31,32] along with two satellite peaks (861.2 eV and 879.7 eV). O 1s spectra in Fig. 6(c) and (d) revealed two peaks in both MNO-0 and MNO-10 nanocomposites at 529.0, 530.7 eV and 529.5, 531.1 eV, and these peaks were related to two oxygen states such as the crystal lattice ($O_{latt.}$) and chemisorbed oxygen specie ($O_{ads.}$), respectively.[33] In Fig. 6(e), Mo 3d spectrum of MNO-10 is displayed, and four peaks at 226.5 eV, 229.2 eV, 232.3 eV, and

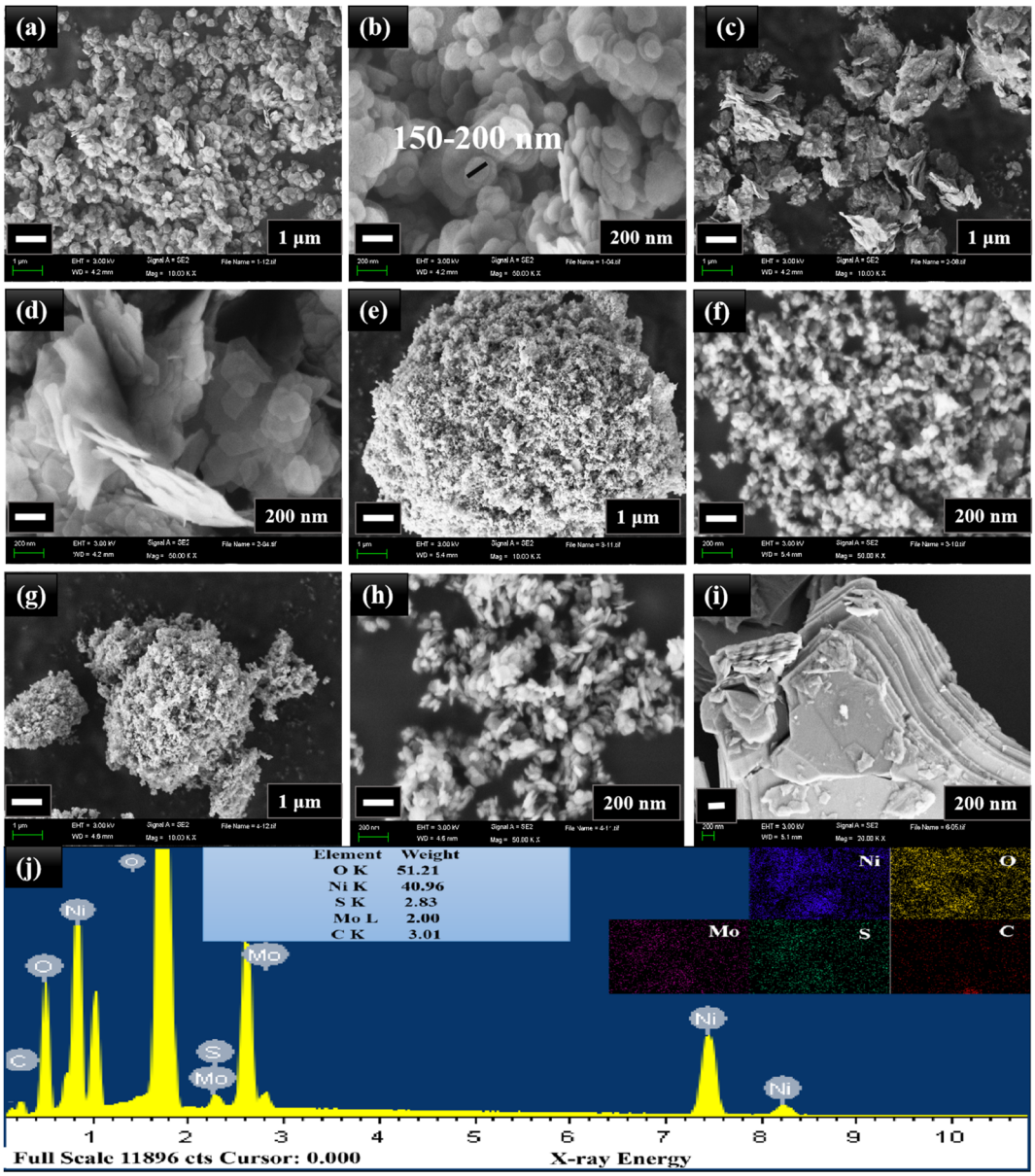

Fig. 3 (a and b) SEM images of MNO-0, (c and d) MNO-5, (e and f) MNO-10, (g and h) MNO-15, and (i) MoS_2. (j) EDS spectrum and mappings of MNO-10.

235.2 eV related to S 2s, Mo^{4+} $3d_{5/2}$, Mo^{4+} $3d_{3/2}$ and Mo^{6+} $3d_{5/2}$.[34,35] In Fig. 6(f), the S 2p spectrum of MNO-10 shows two peaks at 162.1 and 168.3 eV, corresponding to S $2p_{3/2}$ and S $2p_{1/2}$.[36,37] A satellite peak is also displayed in the spectra of S 2p.

3.2 Gas sensing performance

The operating temperature and selectivity are also one of the most important parameters for gas sensor applications. All the gas sensors based on various nanocomposites MNO-*P*, $P = 0$, 5, 10, and 15 showed responses towards 10 ppm H_2S at different temperatures, as shown in Fig. 7. The results proved that the sensors showed the highest responses at room temperature. The sensor of MNO-10 displayed the highest response towards 10 ppm H_2S among all other tested sensors and the response (R_g/R_a) was 6.3, which was 3.15 times that of pure NiO spherical nanoparticles. The results also verified that the response was greatly affected by the operating temperature. When the temperature was increased, the electrons from the semiconductor material surface were likely to break down from the nucleus of the material and form free electrons, which in turn increased the free electron concentration and decreased the resistance as well as the response of the sensor.[3]

The dynamic response transients of MNO-10 towards various H_2S concentrations are shown in Fig. 8(a). The response/recovery times for 10, 6, 5, 4, 3, and 2 ppm were 50/20 s, 45/18 s, 12/16 s, 7/8 s and 6/8 s, respectively. Besides, the response to 2 ppm H_2S was 1.8. In order to spotlight the response/recovery speed towards 10 ppm H_2S, we have placed a graph

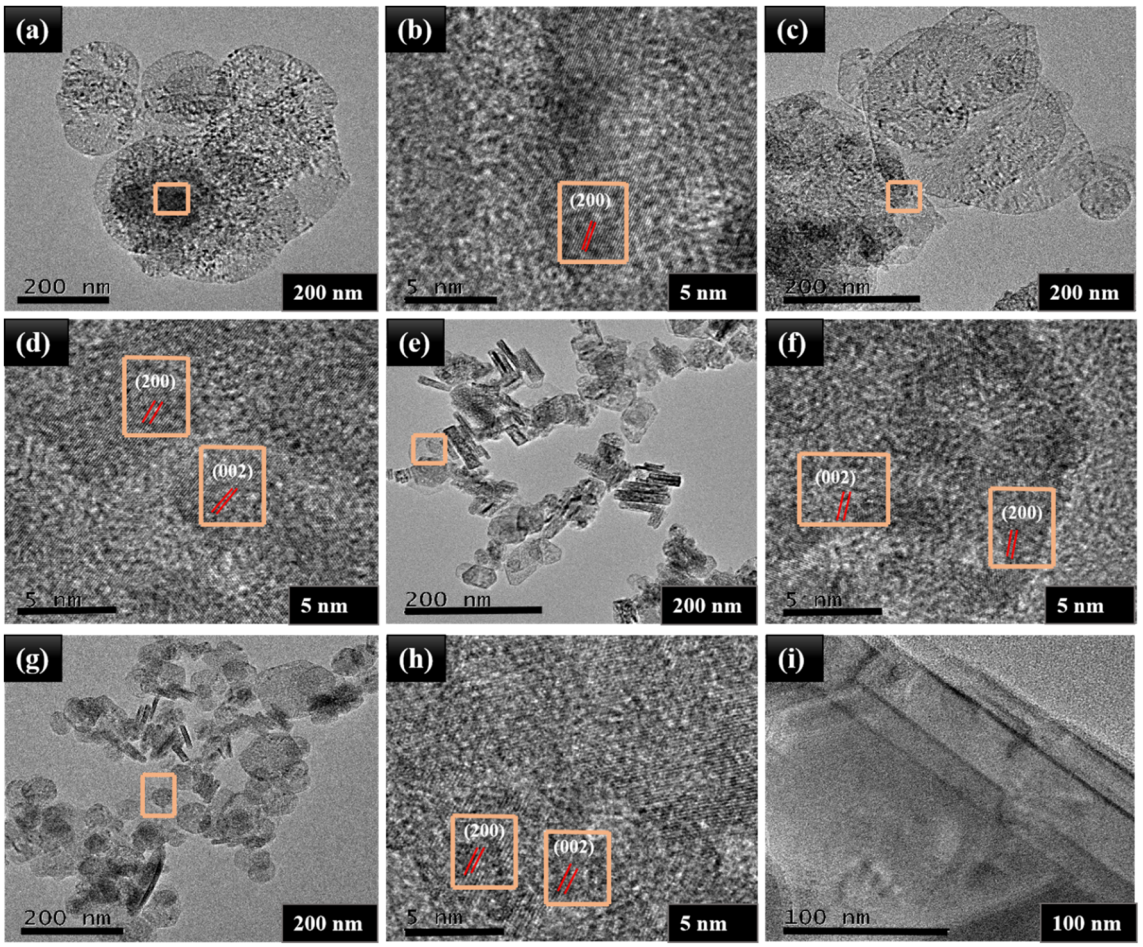

Fig. 4 TEM images and HRTEM images of (a and b) MNO-0, (c and d) MNO-5, (e and f) MNO-10, (g and h) MNO-15, and (i) MoS_2.

between resistance and res./rec. time in Fig. 8(b), which showed that when the sensor was in H_2S atmosphere, the curve went higher (res. time, 50 s) and around (95 000 Ω) it was in the stable state, then in air atmosphere, it started to go back towards the original state (rec. time, 2 s). In Fig. 8(c), the res./rec. times of MNO-10 towards C_4H_{10}, H_2, and NO_2 are shown, with response times 36, 68, and 48 s, and recovery times 26, 40, and 22 for C_4H_{10}, H_2, and NO_2, respectively. The linear relation between

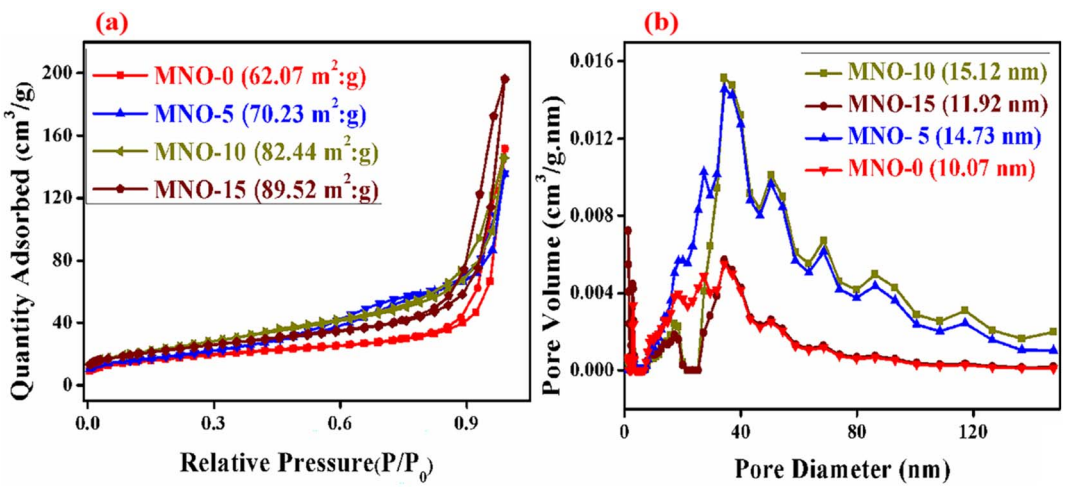

Fig. 5 N_2 adsorption–desorption isotherms and pore size distributions of MNO-0, MNO-5, MNO-10, and MNO-15 (a and b).

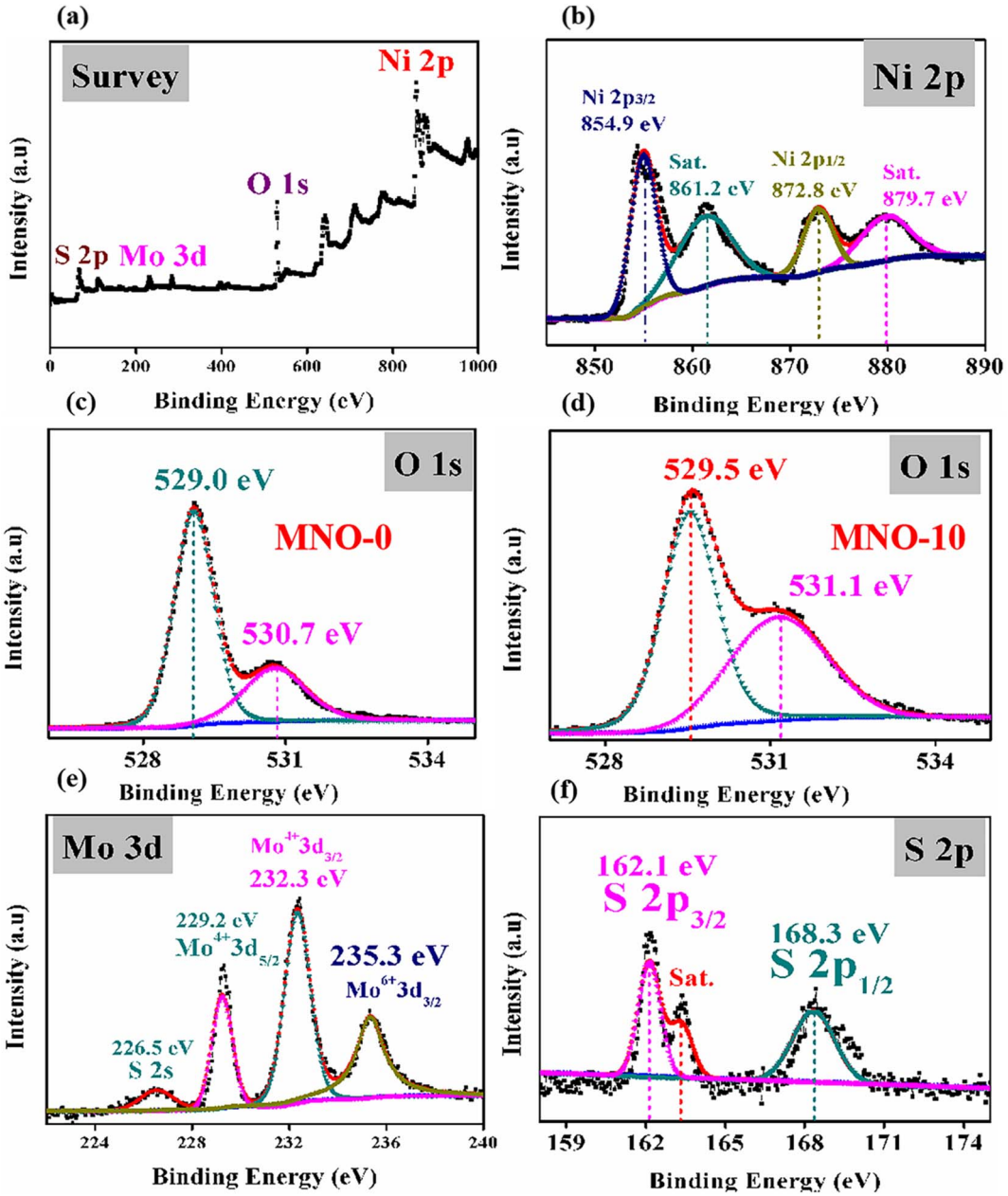

Fig. 6 XPS spectra (a) full survey of MNO-10 (b) Ni 2p spectrum of MNO-10, (c) O 1s spectrum of MNO-0, (d) O 1s spectrum of MNO-10, (e) Mo 3d spectrum of MNO-10, (f) S 2p spectrum of MNO-10.

the response and H_2S ppm is crucial because linearity can make a sensor a promising candidate in gas sensors. Fig. 8(d) shows that the responses of the sensor (MNO-10) were 6.3, 5.1, 4.7, 3.9, 3, 1.9 towards 10, 6, 5, 4, 3, and 2 ppm, respectively, while fitting curve values were 6.7, 5.02, 4.5, 3.8, 3.2, and 2.5 based on the equation of $Y = 1.7735X^{0.5824}$, and regression coefficient, $R^2 = 0.9899$. It is clear from the figure that with increasing H_2S concentrations, the response is gradually increased, suggesting its linearity between the response and H_2S concentrations.

Selectivity is an essential parameter for a gas sensor. In our case, the selectivity of MZCO-*P*, $P = 0$, 5, 10 and 15, based gas sensors was measured, as shown in Fig. 9(a), and the selectivity was checked out using six toxic gases such as H_2S, C_4H_{10}, H_2, NO_2, SO_2, and NH_3 (10 ppm) at RT. The sensor based on MNO-10 showed the response of 6.6, 2.0, 1.9, 2.1, 1.8 and 1.9 towards H_2S, C_4H_{10}, H_2, NO_2, SO_2 and NH_3, respectively. The selectivity of MNO-10 was calculated, such as the ratio of the highest response towards H_2S and the second highest response towards NO_2 (selectivity $= S_{10\ \text{ppm}\ H_2S}/S_{10\ \text{ppm}\ NO_2}$), and its calculated selectivity was around 3. The selectivity of results stated that the response of MNO-10-based gas sensors towards 10 ppm H_2S was almost three times higher than other checked VOCs, which pointed out that the sensor displayed a high response and impressive selectivity towards H_2S. In Table 1, some sensors are

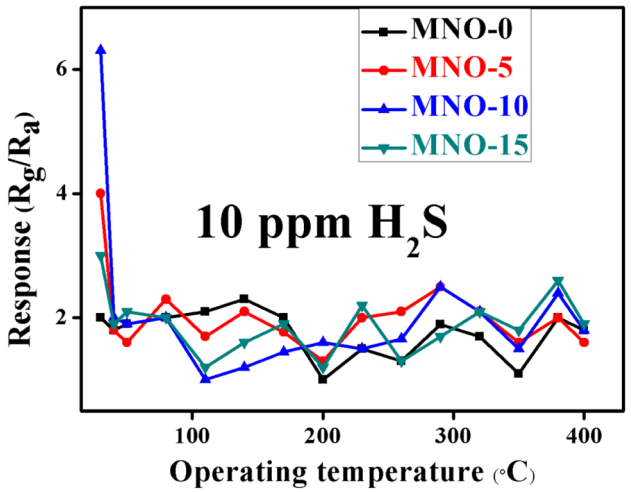

Fig. 7 The responses of various gas sensors at different operating temperatures.

compared against our sensor, which suggests that the current sensor exposed high response (6.3), short response/recovery times (50/20 s), good stability (28 days), better reproducibility (6 cycles), good selectivity (3.0), and linear relationship between response and H_2S concentration. The above features revealed that the simple fabricated sensor in our work is a potential candidate for real-time applications. As far as we know, long-term stability and reproducibility are also imperative for gas sensors. Herein, Fig. 9(b) examines the stability test for all MZCO-*P*, $P = 0$, 3, 6, 9, and 12, nanocomposite-based gas sensors, which showed that the sensors were stable for 28 days. There was no obvious fluctuation in the response with time, exhibiting adequate stability for detecting H_2S at RT. The most stable sensor was the MNO-10-based sensor among all other tested sensors.

For detecting low concentrations of VOCs at RT, high selectivity and good reproducibility are imperative for a sensor to prove its promising applicability. Considering the above factors, reproducibility is also very important. Fig. 10(a) shows the six cycles of the gas sensing performance of MNO-10. As it is clear from the figure, the resistance in gas and air atmosphere was almost the same in six cycles; after every cycle, the resistance can go up in the H_2S atmosphere and back into the air atmosphere, suggesting good reproducibility and reversibility of the current sensor. Fig. 10(b) shows the graph between the response of a sensor based on MNO-10 nanocomposite and relative

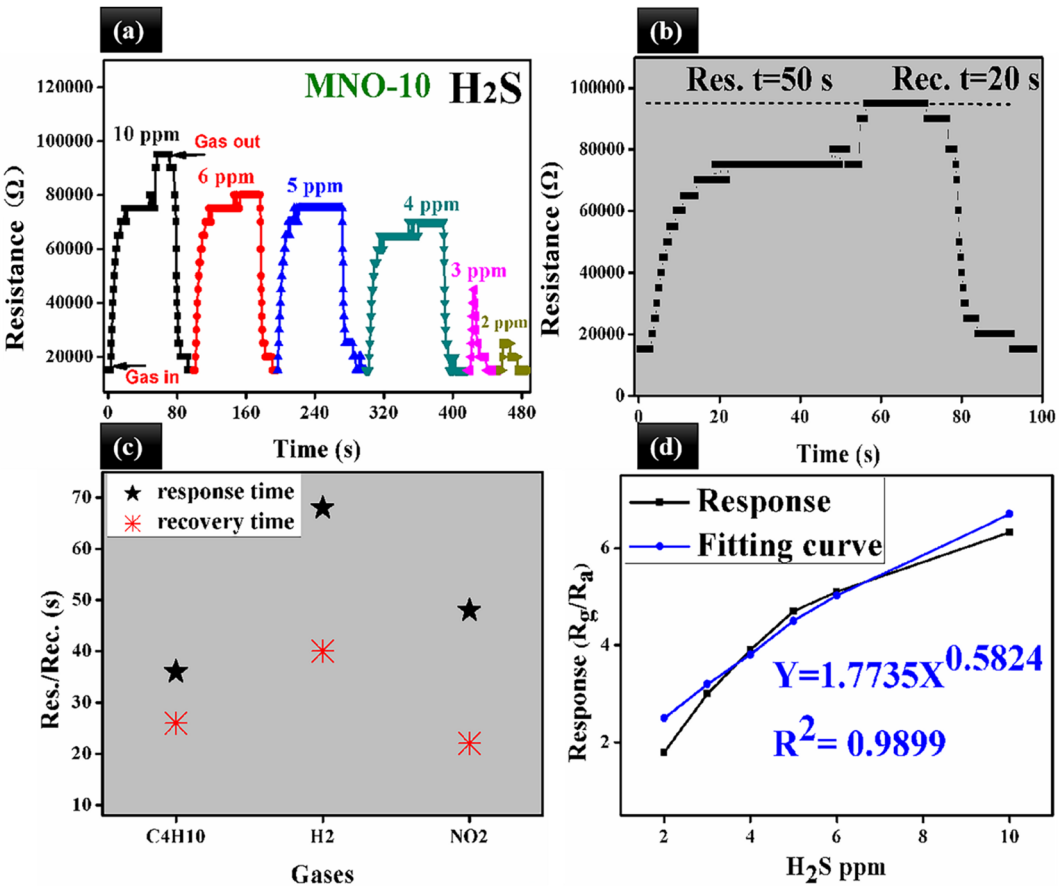

Fig. 8 (a) Dynamic res./rec. curve and resistance of MNO-10 to 10–0.5 ppm H_2S at RT, (b) resistance change of MNO-10 composite-based sensor to 10 ppm H_2S, (c) the plots of response/recovery times towards 10 ppm C_4H_{10}, H_2, and NO_2 of MNO-10, (d) relation between response and different concentrations of H_2S of MNO-10.

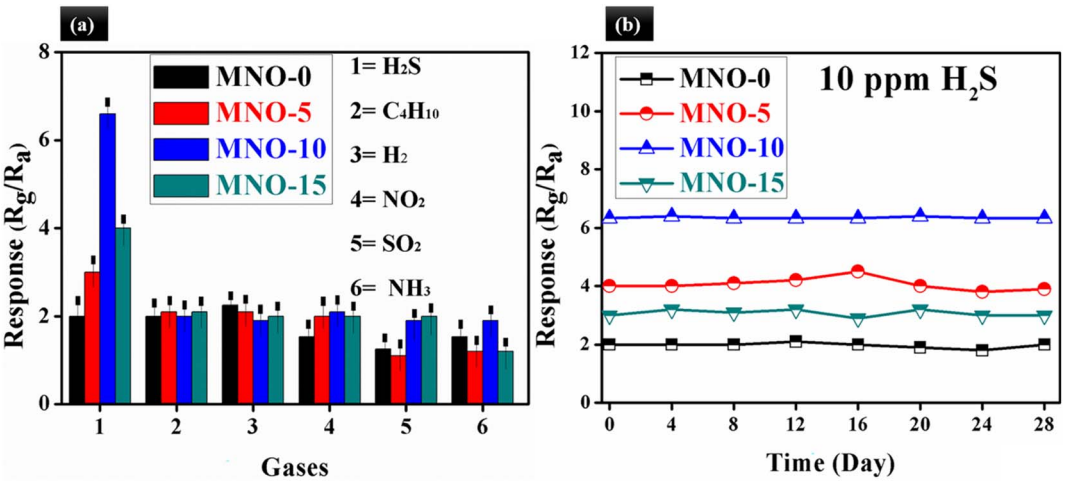

Fig. 9 (a) The selectivity test for all sensors towards various gases at RT, (b) the stability test for all sensors at RT.

humidity (RH). The sensor was tested at RT, and the response was decreased slightly at RH values of 45, 65, and 85, which verified that the sensor has impressive stability against humidity.

3.3 Gas sensing mechanism

We have synthesized a series of nanocomposites based on layered MoS_2 and spherical NiO nanoparticles and applied them as gas sensors, and the highest response towards 10 ppm H_2S was received. For a deeper understanding, the gas sensing mechanism of nanocomposites should be studied, which is required for RT H_2S detection. In general, the gas sensing mechanism is based on the variation of resistance in air and gas environments;[38] however, resistance changes based on the charge carrier concentration of the material surface. In Fig. 11, the gas sensing mechanism and band diagram are described to prove the sensing mechanism. In our experiments, as we can see, the main sample, MNO-10, shows the highest response towards 10 ppm H_2S compared with other tested sensors. The highest response may be correlated to some factors explained as follows: first of all, a p–n hetero-junction is formed between the n-type layered MoS_2 and p-type NiO, which provides a large quantity of electron transfer in the nanostructures; secondly, the layered structure can facilitate the rapid diffusion and electrons transmission density (SEM); third, the layered structure of MoS_2 enhanced the BET surface area of the nanocomposites, which can be considered one of the imperative factors to enhance the gas sensing properties such as high response, good selectivity, and short response/recovery times towards H_2S (BET); fourth, moreover, as XPS approved it, more oxygen species can be adsorbed on the surface of the sensing material, which may help to increase the resistance.

Moreover, as shown in the diagram, when the sensor of MNO-10 was in an air atmosphere, the oxygen molecules were adsorbed on the surface of the material and accepted electrons to convert them into O_2^- (adsorbed oxygen),[39] besides making a hole accumulation layer (HAL) from the holes which are left on the surface, signifying the reduction of resistance. The reactions based on temperatures are described in eqn (1)–(4).

$$O_{2(gas)} \rightarrow O_{2(ads.)}, \quad (1)$$

Table 1 Comparison of various gas sensors[a]

Materials	Operating temp. (°C)	Res./rec. time	Response (gas ppm)	LOD	Stability	Ref.
$PANI/MoS_2/SnO_2$	RT	21 s/130 s	10.9 (NH_3, 100 ppm)	0.2 ppm	—	40
SnO_2/MoS_2	RT	6.8 min/2.7 min	— (NO_2, 10 ppm)	—	—	41
MoS_2	130	1.4 s/2.9 s	86.9 (HCHO, 100 ppm)	10 ppm	30 days	42
NiO/SnO_2	210	—	31.04 (HCHO, 50 ppm)	—	—	43
NiO/ZnO	200	18 s/30 s	9.3 (HCHO, 100 ppm)	—	—	44
NiO/ZnO	240	9 s/8 s	42 (HCHO, 100 ppm)	1 ppm	30 days	31
NiO/ZnO	140	31 s/49 s	142 (glycol, 100 ppm)	—	—	45
$Au–MoS_2$	60	—	10 (NH_3, 1000 ppm)	25 ppm	—	46
rGO/MoS_2	RT	300 s/600 s	— (HCHO, 10 ppm)	—	—	47
$NiCo_2O_4@SnO_2$	160	—	8.87 (ethanol, 100 ppm)	2 ppm	30 days	48
MoS_2–NiO	RT	50 s/29 s	6.3 (H_2S, 10 ppm)	2 ppm	28 days	This work

[a] Temp. = temperature, res./rec. = response/recovery. Ref. = references.

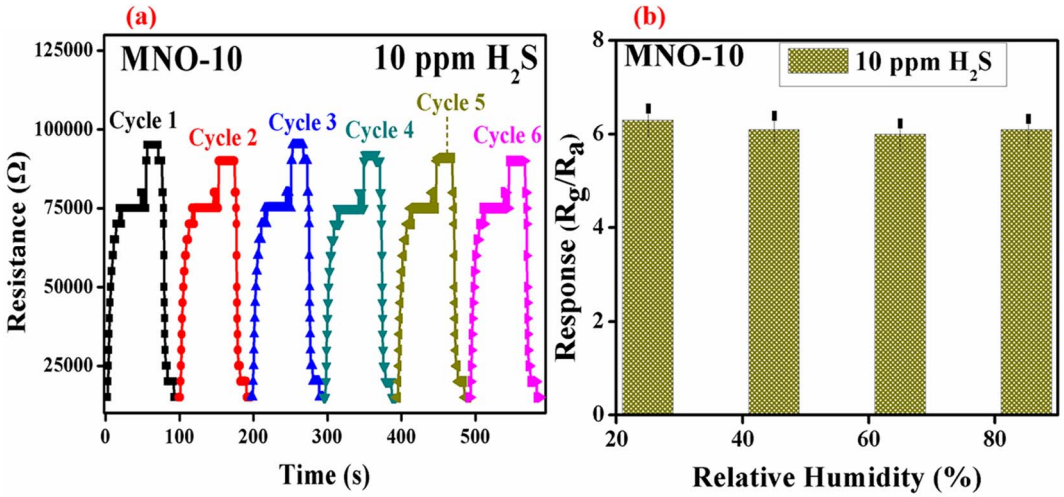

Fig. 10 (a) The reproducibility of MNO-10 based gas sensor at RT towards 10 ppm H_2S, (b) the response *vs.* different RH at RT towards 10 ppm H_2S.

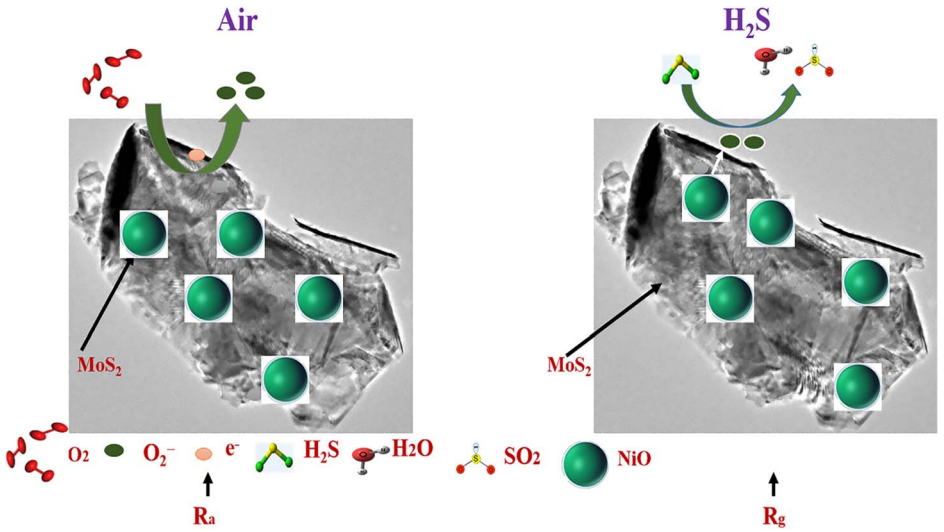

Fig. 11 The gas sensing mechanism and energy band-gap structure of MNO-10 based gas sensor at RT towards 10 ppm H_2S.

$$O_{2(ads.)} + e^- \rightarrow O_{2(ads.)}^-,\ T < 100\ ^\circ C \quad (2)$$

$$O_{2(ads.)}^- + e^- \rightarrow 2O_{(ads.)}^-,\ 100\ ^\circ C \leq T \leq 300\ ^\circ C \quad (3)$$

$$O_{(ads.)}^- + e^- \rightarrow O_{(ads.)}^{2-},\ T > 300\ ^\circ C \quad (4)$$

After that, when the sensor of MNO-10 was in the H_2S atmosphere, the sensor, herein, NiO is a p-type semiconductor. When the sensor was in the H_2S atmosphere, it reacted with O_2^- by forming SO_2 and H_2O, as shown in eqn (5); besides, there was an interaction between the H_2S gas and hydroxyl species of the thin film sensor as well. During the reaction, the electrons returned to the conduction band to recombine holes simultaneously, which decreased the thickness of HAL, increasing the material's resistance. This would improve the gas sensing properties of the current sensor, and MNO-10 showed a p-type behaviour.

$$2H_2S\ (g) + 2O_2^-\ (ads.) \rightarrow 2SO_2 + 2H_2O + 3e^- \quad (5)$$

4. Conclusions

In this study, we designed a new series of sensors based on the nanocomposite of layered MoS_2 and spherical NiO nanoparticles; these nanocomposites were synthesized hydrothermally. Various characterizations were performed, for example, XRD, SEM, TEM, HRTEM, BET, and XPS, to confirm morphology and structural properties. From XRD, it was shown that the crystallite size was reduced with the increase of MoS_2 contents in the nanocomposites, and particle size also decreased by adding MoS_2 (SEM, TEM). Further, BET results proved that the nanocomposites have higher BET-specific surface areas than pure NiO and more oxygen

adsorption of MNO-10 than pure NiO verified by XPS. After that, the synthesized materials were tested as gas sensors, and the gas sensor was fabricated through a mixture of solid and terpineol oil. Various sensors based on nanocomposites (MNO-*A*, $A = 0, 5, 10, 15$) were used for detecting four kinds of toxic gases. The highest response towards 10 ppm H_2S gas was detected by the gas sensor of MNO-10 among all other tested sensors. The response was 6.3 for 10 ppm H_2S. Besides the highest response, the sensor of MNO-10 exposed good selectivity (3.0), better stability (28 days), minimum LOD (2 ppm), good reproducibility (6 cycles), and an almost linear relationship between response and concentrations of H_2S (2–10 ppm). The marvelous gas sensing properties of MNO-10 were related to some crucial points such as p–n hetero-junction, layered structure of MoS_2, higher BET surface area, and increased adsorption of oxygen species. Room temperature H_2S gas sensors fabricated through simple ways are finding novel applications in daily routine activities. In this way, our synthesized nanocomposite-based gas sensor has promising applicability.

Conflicts of interest

This work does not have any conflict of interest.

Acknowledgements

This work was supported by the National Natural Science Foundation of China (51679022), Natural Science Foundation of China (52271303), Dalian Science Technology Innovation Fund (2019J12GX023), Liaoning Revitalization Talents Program (XLYC2002074), Fundamental Research Funds for the Central Universities (3132022219), Fundamental Research Funds for the Central Universities (3132021501), and Technology Innovation Foundation of Dalian (2022JJ11CG010).

References

1 M. D. Shirsat, M. A. Bangar, M. A. Deshusses, N. V. Myung and A. Mulchandani, Polyaniline nanowires-gold nanoparticles hybrid network based chemiresistive hydrogen sulfide gas sensor, *Appl. Phys. Lett.*, 2009, **94**, 083502.

2 N. S. Ramgir, P. K. Sharma, N. Datta, M. Kaur, A. K. Debnath, D. K. Aswal and S. K. Gupta, Room temperature H_2S gas sensor based on Au modified ZnO nanowires, *Sens. Actuators, B*, 2013, **186**, 718–726.

3 X. Li, Y. Zhang, A. Bhattacharya, X. F. Chu, S. Liang and D. Zeng, The formaldehyde sensing properties of $CdGa_2O_4$ prepared by co-precipitation method, *Sens. Actuators, B*, 2021, **343**, 129834.

4 J. Yang, Y. Gui, Y. Wang and S. He, NiO/Ti3C2Tx MXene nanocomposites sensor for ammonia gas detection at room temperature, *J. Ind. Eng. Chem.*, 2023, **119**, 476–484.

5 X. Chen, T. Liu, R. Wu, J. Yu and X. Yin, Gas sensors based on Pd-decorated and Sb-doped SnO2 for hydrogen detection, *J. Ind. Eng. Chem.*, 2022, **115**, 491–499.

6 A. Akhtar, S. Sadaf, J. Liu, Y. Wang, H. Wei, Q. Zhang, C. Fu and J. Wang, Hydro-thermally synthesized spherical g-C_3N_4-$NiCo_2O_4$ nanocomposites for ppb level ethanol detection, *J. Alloys Compd.*, 2022, **911**, 165048.

7 Y. Xiong, Z. Y. Zhu, D. G. Ding, W. B. Lu and Q. Z. Xue, Multi-shelled $ZnCo_2O_4$ yolk-shell spheres for high-performance acetone gas sensor, *Appl. Surf. Sci.*, 2018, **443**, 114–121.

8 K. S. Lee, J. Shim, J. S. Lee, J. Lee, H. G. Moon, Y. J. Park, D. Park and D. I. Son, Adsorption behavior of NO2 molecules in ZnO-mono/multilayer graphene core–shell quantum dots for NO2 gas sensor, *J. Ind. Eng. Chem.*, 2022, **106**, 279–286.

9 S. Verma, P. Mahajan, B. Padha, A. Ahmed and S. Arya, Nanowires based solid-state asymmetric self-charging supercapacitor driven by PVA–ZnO–KOH flexible piezoelectric matrix, *Electrochim. Acta*, 2023, **465**, 142933.

10 V. S. Demin, A. N. Krasovskii, A. M. Lyudchik, V. I. Pokatashkin, I. L. Grigorishin and O. N. Kudanovich, Measurement of ozone over a wide range of concentrations using semiconductor NiO gas sensors, *Meas. Tech.*, 2008, **51**, 1038–1044.

11 S. Choi, J. K. Lee, W. S. Lee, C. Lee and W. I. Lee, Acetone sensing of multi-networked WO3-NiO core-shell nanorods sensors, *J. Korean Phys. Soc.*, 2017, **71**, 487–493.

12 W. Liu, J. Wu, Y. Yang, W. Liu, J. Wu, Y. Yang, H. Yu, X. Dong, X. Wang, Z. Liu, T. Wang and B. Zhao, Facile synthesis of three-dimensional hierarchical NiO microflowers for efficient room temperature H2S gas sensor, *J. Mater. Sci.: Mater. Electron.*, 2018, **29**, 4624–4631.

13 J. Wang, P. Yang, X. Wei and Z. Zhou, Preparation of NiO two-dimensional grainy films and their high-performance gas sensors for ammonia detection, *Nanoscale Res. Lett.*, 2015, **10**, 119.

14 L. Xu, M. Ge, F. Zhang, H. Huang, Y. Sun and D. He, Nanostructured of SnO2/NiO composite as a highly selective formaldehyde gas sensor, *J. Mater. Res.*, 2020, **35**, 3079–3090.

15 J. Li, K. Yu, Y. Tan, H. Fu, Q. Zhang, W. Cong, W. Cong, C. Song, H. Yin and Z. Zhu, Facile synthesis of novel MoS_2@SnO_2 hetero-nanoflowers and enhanced photocatalysis and field-emission properties, *Dalton Trans.*, 2014, **43**, 13136–13144.

16 L. Chen, M. Arshad, Y. Chuang, T. B. Nguyen, C. H. Wu, C. W. Chen and C. D. Dong, A novel nano-heterojunction MoS2/α-Fe2O3 photocatalysts with high photocatalytic and photoelectrochemical performance under visible light irradiation, *J. Alloys Compd.*, 2023, **947**, 169577.

17 M. Mohan, N. P. Shetti and T. M. Aminabhavi, Phase dependent performance of MoS2 for supercapacitor applications, *J. Energy Storage*, 2023, **58**, 106321.

18 H. He, Z. Liu, C. Peng, J. Liu, X. Wang and J. Zeng, 3D MoS2/graphene nanoflowers as anode for advanced lithium-ion batteries, *Trans. Nonferrous Met. Soc. China*, 2022, **32**, 4041–4049.

19 M. Mansha, A. Qureshi, N. Ullah, F. O. Bakare, I. Khan and Z. H. Yamani, Synthesis of In_2O_3/graphene heterostructure

and their hydrogen gas sensing properties, *Ceram. Int.*, 2016, **42**, 11490–11495.

20 D. Wu, S. Sadaf, H. Zhang and A. Akhtar, Sub-ppm level ethanol detection based on the gas sensor of g-C3N4-ZnO-Zn2SnO4 nanocomposite, *Chem. Phys. Lett.*, 2023, **817**, 140425.

21 H. I. Hamouda, H. M. Abdel-Ghafar and M. H. H. Mahmoud, Multi-walled carbon nanotubes decorated with silver nanoparticles for antimicrobial applications, *J. Environ. Chem. Eng.*, 2021, **9**, 105034.

22 A. Sharma, A. Singh, V. Gupta, A. K. Sundramoorthy and S. Arya, Involvement of metal organic frameworks in wearable electrochemical sensor for efficient performance, *Trends Environ. Anal. Chem.*, 2023, **38**, e00200.

23 A. Ahmed, S. Verma, P. Mahajan, A. K. Sundramoorthy and S. Arya, Upcycling of surgical facemasks into carbon based thin film electrode for supercapacitor technology, *Sci. Rep.*, 2023, **13**, 12146.

24 Y. Li, X. Song, L. Li, W. Wu, K. Tao, Z. Ying, Y. Hu, Y. Zhou, R. Zhang, G. Wang and F. Wen, Low concentration CO gas sensor constructed from MoS2 nanosheets dispersed SnO2 nanoparticles at room temperature under UV light, *Ceram. Int.*, 2023, **49**, 10249–10254.

25 H. Bai, H. Guo, C. Feng, J. Wang, B. Liu, Z. Xie, F. Guo, D. Chen, R. Zhang and Y. Zheng, Light-activated ultrasensitive NO2 gas sensor based on heterojunctions of CuO nanospheres/MoS2 nanosheets at room temperature, *Sens. Actuators, B*, 2022, **368**, 132131.

26 R. R. Kumar, T. Murugesan, A. Dash, C. H. Hsu, S. Gupta, A. Manikandan, A. K. Anbalagan, C. H. Lee, N. H. Tai, Y. Chueh and H. N. Lina, Ultrasensitive and light-activated NO2 gas sensor based on networked MoS2/ZnO nanohybrid with adsorption/desorption kinetics study, *Appl. Surf. Sci.*, 2021, **536**, 147933.

27 J. Hu, X. Liu, J. Zhang, X. Gu and Y. Zhang, Plasmon-activated NO2 sensor based on Au@MoS2 core-shell nanoparticles with heightened sensitivity and full recoverability, *Sens. Actuators, B*, 2023, **382**, 133505.

28 D. Wu and A. Akhtar, Ppb-Level Hydrogen Sulfide Gas Sensor Based on the Nanocomposite of MoS_2 Octahedron/ZnO-Zn_2SnO_4 Nanoparticles, *Molecules*, 2023, **28**, 3230.

29 T. T. H. Duong, H. H. Hau, L. T. Hong, L. A. Vu, C. M. Hung, N. V. Duy, N. V. Hieu and N. D. Hoa, PtO2-decorated MoS2 ultrathin nanostructures for enhanced NH3 gas sensing properties, *Mater. Sci. Semicond. Process.*, 2022, **151**, 106990.

30 R. BoopathiRaja, M. Parthibavarman and A. N. Begum, Hydrothermal induced novel $CuCo_2O_4$ electrode for high performance super-capacitor applications, *Vacuum*, 2019, **165**, 96–104.

31 B. Li, H. Liu, Q. Zeng, S. Dong and W. Feng, Hierarchical porous NiO doped ZnO nanocomposite for formaldehyde gas sensor with high sensitivity, fast response/recovery and good selectivity, *Surf. Interfaces*, 2023, **36**, 102502.

32 T. Pushpagiri, E. R. Kumar, A. Ramalingam, A. F. Abd El-Rehim and C. Srinivas, Effect of doping concentration on structural, vibrational, morphological and colloidal stability of Zn doped NiO nanoparticles for gas sensor applications, *Ceram. Int.*, 2023, **49**, 23903–23911.

33 Y. Xiong, Q. Xue, C. Ling, W. Lu, D. Ding, L. Zhu and X. Li, Effective CO_2 detection based on LaOCl-doped SnO_2 nanofibers: insight into the role of oxygen in carrier gas, *Sens. Actuators, B*, 2017, **241**, 725–734.

34 W. J. Zhou, Z. Y. Yin, Y. P. Du, X. Huang, Z. Y. Zeng, Z. X. Fan, H. Liu, J. Y. Wang and H. Zhang, Synthesis of few-layer MoS_2 nanosheet-coated TiO_2 nanobelt heterostructures for enhanced photocatalytic activities, *Small*, 2013, **9**, 140–147.

35 P. X. Zhao, Y. Tang, J. Mao, Y. X. Chen, H. Song, J. W. Wang, Y. Song, Y. Q. Liang and X. M. Zhang, One-dimensional MoS_2-decorated TiO_2 nanotube gas sensors for efficient alcohol sensing, *J. Alloys Compd.*, 2016, **674**, 252–258.

36 S. M. Cui, Z. H. Wen, X. K. Huang, J. B. Chang and J. H. Chen, Stabilizing MoS_2 nanosheets through SnO_2 nanocrystal decoration for high-performance gas sensing in air, *Small*, 2015, **11**, 2305–2313.

37 M. Manuraj, J. Chacko, K. N. N. Unni and R. B. Rakhi, Heterostructured MoS_2-RuO_2 nanocomposite: a promising electrode material for super capacitors, *J. Alloys Compd.*, 2020, **836**, 155420.

38 W. Q. Li, S. Y. Ma, Y. F. Li, X. B. Li, C. Y. Wang, X. H. Yang, L. Cheng, Y. Z. Mao, J. Luo, D. J. Gengzang, G. X. Wan and X. L. Xu, Preparation of Pr-doped SnO2 hollow nanofibers by electrospinning method and their gas sensing properties, *J. Alloys Compd.*, 2014, **605**, 80–88.

39 H. P. Dai, N. N. Feng, J. W. Li, J. Zhang and W. Li, Chemiresistive humidity sensor based on chitosan/zinc oxide/single-walled carbon nanotube composite film, *Sens. Actuators, B*, 2019, **283**, 786–792.

40 A. Liu, S. Lv, L. Jiang, F. Liu, L. Zhao, J. Wang, X. Hu, Z. Yang, J. He, C. Wang, X. Yan, P. Sun, K. Shimanoe and G. Lu, The gas sensor utilizing polyaniline/MoS_2 nanosheets/SnO_2 nanotubes for the room temperature detection of ammonia, *Sens. Actuators, B*, 2021, **332**, 129444.

41 S. Cui, Z. Wen, X. Huang, J. Chang and J. Chen, Stabilizing MoS_2 Nanosheets through SnO_2 Nanocrystal Decoration for High-Performance Gas Sensing in Air, *Small*, 2015, **11**, 2305–2313.

42 G. J. Choi, R. K. Mishra and J. S. Gwag, 2D layered MoS_2 based gas sensor for indoor pollutant formaldehyde gas sensing applications, *Mater. Lett.*, 2020, **264**, 127385.

43 S. Das, A. Kumar, J. Singh and M. Kumar, Fabrication and modeling of laser ablated NiO nanoparticles decorated SnO2 based formaldehyde sensor, *Sens. Actuators, B*, 2023, **387**, 133824.

44 X. San, M. Li, D. Liu, G. Wang, Y. Shen, D. Meng and F. Meng, A facile one-step hydrothermal synthesis of NiO/ZnO heterojunction microflowers for the enhanced formaldehyde sensing properties, *J. Alloys Compd.*, 2018, **739**, 260–269.

45 C. Su, L. Zhang, Y. Han, C. Ren, B. Li, T. Wang, M. Zeng, Y. Su, N. Hu, Z. Zhou, Y. Wang, Z. Yang and L. Xu, Glucose-assisted synthesis of hierarchical NiO-ZnO heterostructure with enhanced glycol gas sensing performance, *Sens. Actuators, B*, 2021, **329**, 129167.

46 H. Yan, P. Song, S. Zhang, J. Zhang, Z. Yang and Q. Wang, A low temperature gas sensor based on Au-loaded MoS_2 hierarchical nanostructures for detecting ammonia, *Ceram. Int.*, 2016, **42**, 9327–9331.
47 X. Li, J. Wang, D. Xie, J. Xu, Y. Xia, W. Li, L. Xiang, Z. Li, S. Xu and S. Komarneni, *Nanotechnology*, 2017, **28**, 325501.
48 Q. Wang, J. Bai, B. Huang, Q. Hu, X. Cheng, J. Li, E. Xie, Y. Wang and X. Pan, Design of $NiCo_2O_4$@SnO_2 hetero structure nanofiber and their low temperature ethanol sensing properties, *J. Alloys Compd.*, 2019, **791**, 1025–1032.